INORGANIC CHEMISTRY FRONTIERS

RESEARCH ARTICLE

View Article Online
View Journal | View Issue

Cite this: *Inorg. Chem. Front.*, 2024, **11**, 6960

Modulation of the near-infrared-I and -II luminescence of thulium-incorporated lead-free double perovskites†

Jingheng Nie,[a] Weitao Ying,*[b] Renping Cao,[a] Sijie Liu,[a] Shaobin Qiu,[c] Chaohong Liao,[a] Xiangyan Yun,[d] Bang Lan*[a] and Jing Wang *[a,e]

Currently, lanthanide-doped metal halide perovskites with near-infrared (NIR) luminescence are receiving considerable attention. However, they suffer from low NIR efficiency, particularly in the NIR-II emission range, and are primarily excited by high-energy ultraviolet light. In this work, high-performance NIR-I and -II emissions were realized by co-doping a $Cs_2NaInCl_6$ lattice with Tm^{3+} ions as luminescent emitters and Sb^{3+} and Te^{4+} ions as sensitizer ions, where Sb^{3+} ions can enable short-wavelength high-energy excitation and Te^{4+} ions can enable long-wavelength blue-light excitation. The NIR photoluminescence quantum yield (PLQY) reaches an unprecedented 58.0% in $Cs_2NaInCl_6$:Sb^{3+}/Tm^{3+} (NIR-II emission: 1224 nm–48.9%), which is attributed to the presence of the $^1G_4$ energy level of the Tm^{3+} ion acting as a bridge, efficiently transferring energy from high-energy states of Sb^{3+} to NIR-emissive states. Moreover, Tm^{3+} ions can be sensitized by Te^{4+} ions that have broadband absorption in the blue region, which enable a high NIR PLQY of 10.3% in $Cs_2NaInCl_6$:Te^{4+}/Tm^{3+} under 420 nm excitation. The excellent NIR luminescence performance combined with excellent environmental stability endows $Cs_2NaInCl_6$:Sb^{3+}/Tm^{3+} and $Cs_2NaInCl_6$:Te^{4+}/Tm^{3+} with considerable potential for application in night-vision devices.

Received 16th July 2024,
Accepted 28th August 2024

DOI: 10.1039/d4qi01772b

rsc.li/frontiers-inorganic

Introduction

Near-infrared-I (NIR-I: 700–1000 nm) and near-infrared-II (NIR-II: 1000–1400 nm) luminescence is crucial in various fields related to human activities due to their low thermal effect, nondestructive nature, and suitable penetration.[1–4] The prevailing commercial NIR light sources including halogen and tungsten lamps are plagued by multiple shortcomings such as low efficiency, bulky design, and brief operational lifespans, providing the impetus for developing new high-performance NIR emitters.[5,6] Traditionally, trivalent chromium (Cr^{3+} ion)-doped phosphors have been considered desirable NIR emitters; however, most of the reported Cr^{3+} emissions only partially cover the NIR region, and the rest of them are located within the far-red region.[7–12] Nevertheless, lanthanide (Ln^{3+}) doping enables them to emit various wavelengths of the NIR regions, taking advantage of their abundant metastable excitation energy levels.[13–15] In particular, for emerging optical communication technologies, NIR emissions at around 1.2 μm for the $^3H_5 \rightarrow {}^3H_6$ electron transition of Tm^{3+} ions are more attractive. Several of these Ln^{3+}-doped NIR emitters have been successfully commercialized. However, Ln^{3+}-doped NIR emitters generally suffer from weak light absorption confined by forbidden f–f transitions.[16,17] Therefore, sensitizing Ln^{3+} luminescence by constructing appropriate energy transfer channels is expected to be an effective strategy to achieve efficient NIR-I and NIR-II emissions.

Recently, lead-free metal halide double perovskites have been explored as hosts for doping with Ln^{3+} to generate NIR photoluminescence (PL), which has gained tremendous interest for extensive research in the field of photoelectric

[a]*Northeast Guangdong Key Laboratory of New Functional Materials, School of Chemistry and Environment, Jiaying University, Meizhou, 514015, P. R. China. E-mail: jyulb6@163.com, ceswj@mail.sysu.edu.cn*
[b]*Department of Chemistry, Hengshui University, Hengshui, Hebei 053500, P. R. China. E-mail: 601706@hsnc.edu.cn*
[c]*School of Physics and Electrical Engineering, Jiaying University, Meizhou, 514015, P. R. China*
[d]*International Collaborative Laboratory of 2D Materials for Optoelectronics Science and Technology of Ministry of Education, Institute of Microscale Optoelectronics, Shenzhen University, Shenzhen 518060, P. R. China*
[e]*Ministry of Education Key Laboratory of Bioinorganic and Synthetic Chemistry, State Key Laboratory of Optoelectronic Materials and Technologies, Sun Yat-Sen University, Guangzhou, Guangdong 510275, P. R. China*

†Electronic supplementary information (ESI) available: Detailed description of the experimental synthesis, and characterizations; XRD pattern, ultraviolet–visible absorption spectra, PL decay curves, PLE spectra, PL spectra, PLQY, DOS, photoluminescence stability, ICP elemental analysis (PDF). See DOI: https://doi.org/10.1039/d4qi01772b

materials,[18–24] since halide double perovskites can provide octahedral coordination (CN = 6), which is beneficial for Ln^{3+} incorporation. For example, Nag *et al.* doped Yb^{3+}/Er^{3+} into $Cs_2AgInCl_6$ double perovskites, and the NIR emissions at 994 and 1550 nm from doped ions were realized.[25] Unfortunately, the NIR PL quantum yield (PLQY) of these Ln^{3+}-doped $Cs_2AgInCl_6$ is not satisfactory owing to the inefficient energy transfer. Although many studies have reported the sensitization and enhancement of Ln^{3+}-related NIR emission by the energy transfer from self-trapped excitons (STEs) to Ln^{3+} ions, the sensitization efficiency and luminescence of Ln^{3+} ions are low and weak because STEs take away part of the absorbed energy and cannot efficiently transfer their energy to Ln^{3+} ions. Due to the lack of resonance condition (limited overlap between STE emission and Ln^{3+} absorption profiles), tuning the emission spectra of the sensitized centers for better resonance with suitable Ln^{3+} ions is well worth exploring. Currently, the NIR-II emission of Ln^{3+} ions in reported double perovskites still suffers from the problems of low efficiency and high-energy ultraviolet light excitation, which considerably hinders their further application.[21,22,26,27] In this regard, it remains an important material design challenge to modulate the excitation and emission energies while investigating and optimizing the energy transfer efficiency in conjunction with the different energy level structures of Ln^{3+} ions to improve the power conversion efficiency of such NIR-II emitters.

In this work, high-performance NIR-I and NIR-II light was realized by co-doping Tm^{3+} and sensitizer ions (Sb^{3+} and Te^{4+}) into a $Cs_2NaInCl_6$ lattice where Sb^{3+} ions can enable short-wavelength high-energy excitation and Te^{4+} ions can enable long-wavelength low-energy excitation. Through Sb^{3+} sensitization, efficient NIR-I emission at 808 nm and NIR-II emission at 1224 nm with a high NIR PLQY of up to 58.0% was realized in $Cs_2NaInCl_6$:Sb^{3+}/Tm^{3+} under 320 nm excitation. The energy transfer efficiency in the Sb^{3+}/Tm^{3+} co-doped sample is up to 56.1%, which may be attributed to the relatively large overlap between Sb^{3+} emission and Tm^{3+} absorption profiles. The presence of the $^1G_4$ energy level of the Tm^{3+} ion acts as a bridge, facilitating the transfer of energy from Sb^{3+} to Tm^{3+}. Based on the sensitization of Te^{4+} ions, similar NIR emissions with a high NIR PLQY of up to 10.3% have been realized in $Cs_2NaInCl_6$:Te^{4+}/Tm^{3+} under blue light 420 nm excitation. The experiments and DFT calculations reveal the origin of the luminescence and demonstrate the possibility of energy transfer. Profiting from the efficient energy transfer channels, highly efficient NIR-I and NIR-II emissions of Tm^{3+} ions can be realized. The excellent NIR-I and NIR-II luminescence performance combined with excellent environmental stability endows $Cs_2NaInCl_6$:Sb^{3+}/Tm^{3+} and $Cs_2NaInCl_6$:Te^{4+}/Tm^{3+} with great potential for application in night-vision devices. This work provides inspiration for the design of excitation state modulation and efficient NIR-emitting Ln^{3+}-doped halide perovskites, demonstrating their considerable potential as NIR LEDs for night vision technologies and other related fields.

Results and discussion

The $Cs_2NaInCl_6$ double perovskite is environmentally friendly and serves as an excellent host material owing to the wide bandgap that does not interact with most of the ultraviolet-visible radiation, resulting in photostability. We obtained Tm^{3+}-doped halide double crystals by a hydrothermal method. The corresponding structures of $Cs_2NaInCl_6$ and $Cs_2NaInCl_6$:Tm^{3+}–Sb^{3+} (or Te^{4+}) double perovskites are shown in Fig. 1a, where Tm^{3+}, Sb^{3+}, and Te^{4+} randomly occupy the position of In^{3+} when doped into the lattice. The powder X-ray diffraction (XRD) patterns of the samples show that the XRD patterns of $Cs_2NaInCl_6$:Sb^{3+}/Tm^{3+} and $Cs_2NaInCl_6$:Te^{4+}/Tm^{3+} samples can correspond well to the standard card (ICSD#132718), as shown in Fig. 1b. The diffraction peaks of Sb^{3+}/Tm^{3+} or Te^{4+}/Tm^{3+}-doped samples shift toward a lower angle as the Tm^{3+} concentration increases, as shown in Fig. S1.† This shift occurs because the ionic radius of Tm^{3+} (88 pm) is larger than that of In^{3+} (80 pm), which indicates that Tm^{3+} was successfully doped into the lattice. The actual doping concentrations were determined by inductively coupled plasma mass spectrometry (ICP-MS), and the results are listed in Tables S1 and S2.†

The PL excitation (PLE) and PL spectra of $Cs_2NaInCl_6$ doped with different types of ions are studied to explore the luminescence properties of Tm^{3+} ion-doping systems. The PLE spectra of both Sb^{3+} and Sb^{3+}/Tm^{3+}-doped $Cs_2NaInCl_6$ samples have a strong excitation band at around 320 nm (Fig. 2a), corresponding to the $^1S_0 \rightarrow {}^3P_1$ transition of Sb^{3+}.[28,29] The Sb^{3+}

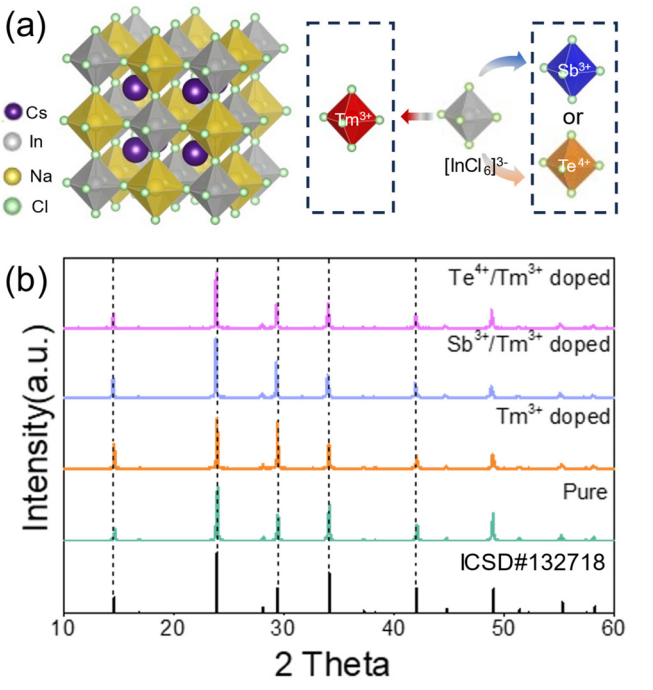

Fig. 1 (a) Structural schematic diagram of $Cs_2NaInCl_6$, $Cs_2NaInCl_6$:Sb^{3+}/Tm^{3+}, and $Cs_2NaInCl_6$:Te^{4+}/Tm^{3+} double perovskites. (b) XRD patterns of pure, 5%Sb^{3+}/30%Tm^{3+}, and 1%Te^{4+}/30%Tm^{3+} doped $Cs_2NaInCl_6$.

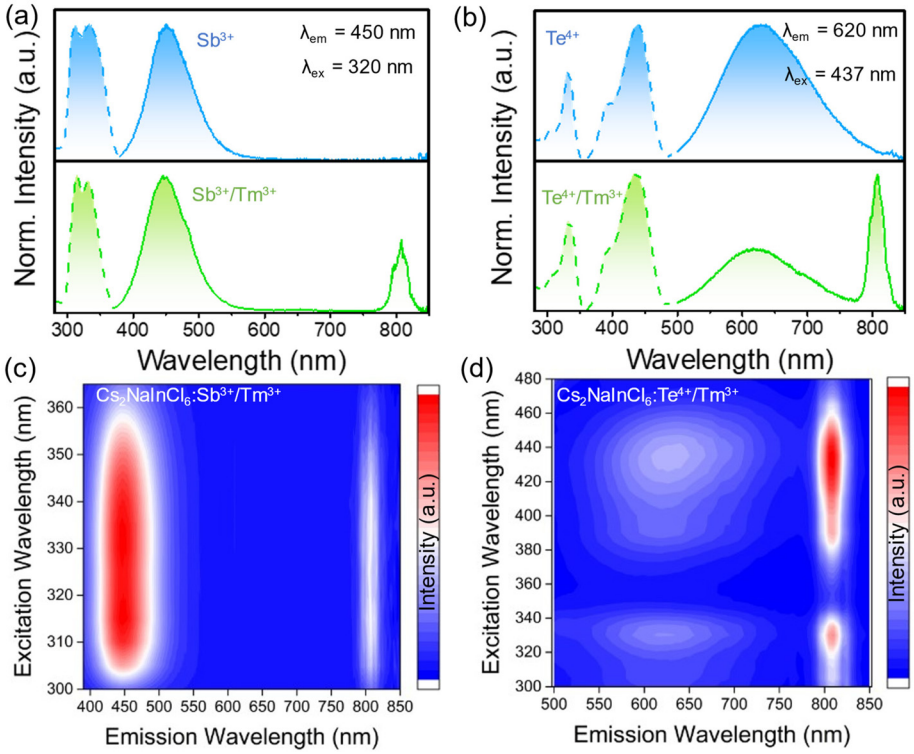

Fig. 2 (a) PLE and PL spectra of 5%Sb^{3+} and 5%Sb^{3+}/60%Tm^{3+}-doped $Cs_2NaInCl_6$. (b) PLE and PL spectra of 1%Te^{4+} and 1%Te^{4+}/50%Tm^{3+}-doped $Cs_2NaInCl_6$. The PLE/PL mapping of (c) 5%Sb^{3+}/60%Tm^{3+} and (d) 1%Te^{4+}/50%Tm^{3+}-doped $Cs_2NaInCl_6$.

single-doped $Cs_2NaInCl_6$ samples exhibit a broadband blue emission at 450 nm under 320 nm excitation, while Sb^{3+}/Tm^{3+}-doped $Cs_2NaInCl_6$ samples exhibit considerable NIR-I emission peaks at 808 nm, where the 808 nm NIR-I emission is attributed to the f–f transition process of Tm^{3+} ions.[27] The doping of Tm^{3+} ions can induce the NIR luminescence of $Cs_2NaInCl_6$ perovskite materials. The PL/PLE pseudo-color maps demonstrate that the excited state origin of these emission bands was the same (Fig. 2c), suggesting that the NIR luminescence of Tm^{3+} ions primarily depends on the sensitization of Sb^{3+} ions.

Although NIR luminescence can be achieved in the Sb^{3+}/Tm^{3+} systems, the excitation energy is high; therefore, we introduced other sensitizers to modulate the excitation wavelength. The PLE spectra of $Cs_2NaInCl_6$ samples doped with Te^{4+} and Te^{4+}/Tm^{3+} exhibit similar excitation bands, with the optimal excitation wavelength appearing at 437 nm (Fig. 2b). The PLE peak closely agrees with the absorption spectrum and has a strong absorption cross-section with the addition of sensitizers (Fig. S2†). The Te^{4+} singly doped $Cs_2NaInCl_6$ sample exhibits a broadband emission at 620 nm under 437 nm excitation with a full width at half maximum of 152 nm, which was attributed to the Te^{4+}-state *via* $^3P_{0,1} \rightarrow {}^1S_0$ transition or related STE emission.[30,31] The Te^{4+}/Tm^{3+}-doped $Cs_2NaInCl_6$ sample demonstrates an additional NIR-I emission peak at 808 nm, which is attributed to the electronic transition process of Tm^{3+} ions. Accordingly, the NIR emission exhibited a millisecond-scale lifetime of 2.91 ms for Sb^{3+}/Tm^{3+} and 3.23 ms for Te^{4+}/Tm^{3+} (Fig. S3†), which is attributed to Laporte forbidden f–f transitions. The introduction of Tm^{3+} ions could reduce the broadband emission intensity (500–800 nm) while generating NIR emission. The PL/PLE pseudo-color maps confirm that the excited state origin of these emission bands was the same (Fig. 2d), indicating that the energy transfer process through Te^{4+} is the main pathway to achieve NIR emission of Tm^{3+} ions.

In addition to introducing Te^{4+} ion sensitizers to achieve long-wavelength excitation, we introduced other ions in addition to the original Sb^{3+}/Tm^{3+} doping to modulate the excited state of Sb^{3+}. After introducing Bi^{3+} ions, the PLE of $Cs_2NaInCl_6$:Sb^{3+}/Bi^{3+}/Tm^{3+} splits further, with the splitting width caused by the Jahn–Teller deformation increasing with Bi^{3+} ion concentration (Fig. S4†). With the increase in Bi^{3+} ion doping concentration, the excitation peak can be effectively modulated from 330 to 360 nm, although the luminescence intensity is slightly reduced, as shown in Fig. S5.† Furthermore, the introduction of Bi^{3+} into the Te^{4+}/Tm^{3+} system did not change the spectra, and the excitation peaks were consistent with those of Te^{4+} and the Te^{4+}/Tm^{3+} doping systems (Fig. S6†), indicating that the introduction of Bi^{3+} did not modulate the excited state of Te^{4+}.

To explore the effect of Tm^{3+} ion doping concentration on the luminescence performance of samples, the emission spectra of $Cs_2NaInCl_6$:Sb^{3+}/Tm^{3+} and $Cs_2NaInCl_6$:Te^{4+}/Tm^{3+}

are recorded at different Tm^{3+} ion doping concentrations (Fig. 3a and b). $Cs_2NaInCl_6$:Sb^{3+} only demonstrates a strong broadband blue emission peak, which could be attributed to the inter-configurational transitions of Sb^{3+} dopants.[26,32] After introducing Tm^{3+} ions, the PL spectra exhibit a distinct NIR-I emission peak attributed to the $^3H_4 \rightarrow {}^3H_6$ electron transition process of Tm^{3+} ions under ultraviolet (UV) light excitation. The detailed trends of blue and NIR-I emission intensities of the $Cs_2NaInCl_6$:Sb^{3+}/Tm^{3+} sample with the increase in Tm^{3+} doping concentration are shown in Fig. 3c. Under excitation of 320 nm, the NIR emission of Tm^{3+} ions gradually increased with the increase in Tm^{3+} concentration. However, the intensity of the blue emission of Sb^{3+} decreases, indicating the presence of energy transfer process from Sb^{3+} to Tm^{3+} in $Cs_2NaInCl_6$ perovskites. Similarly, the $Cs_2NaInCl_6$:Te^{4+}/Tm^{3+} sample exhibits a NIR-I emission peak at 808 nm (Tm^{3+}: $^3H_4 \rightarrow {}^3H_6$) on the basis of the broadband emission peak of Te^{4+} with the introduction of Tm^{3+} ions. As shown in Fig. 3d, the Te^{4+} emission intensity decreased, while the NIR emission intensity greatly increases for up to 50% Tm^{3+} doping. Higher doping concentrations lead to a decrease in NIR efficiency, which is caused by concentration quenching.

In addition to the NIR-I emission at 808 nm, we found that the Tm^{3+} ion-doped samples exhibited intense NIR-II emissions at 1224 nm, which was attributed to the $^3H_5 \rightarrow {}^3H_6$ electron transition process of Tm^{3+} ions. As shown in Fig. 4a, the NIR-II emission intensity considerably increases for up to 60% Tm^{3+} doping. The PLE spectra of NIR-II emission show the same profiles, which indicate that the NIR-II emission could originate from Sb^{3+} ions (Fig. 4b). The NIR emission spectra were almost constant with the variation in the excitation wavelength (Fig. 4c), indicating that the NIR-II luminescence of Tm^{3+} ions primarily depends on the sensitization of Sb^{3+} ions. Similarly, the Te^{4+}/Tm^{3+}-codoped $Cs_2NaInCl_6$ exhibited the same NIR-II emission, with the NIR-II emission intensity increasing for up to 50% Tm^{3+} doping, as shown in Fig. 4d. The PLE spectra of NIR-II emission show the same profiles, indicating that the NIR-II emission could originate from Te^{4+} ions (Fig. 4e). The PL and PLE pseudo-color maps confirm that the NIR-II emission is realized by an energy transfer process from Te^{4+} to Tm^{3+} ions (Fig. 4f). The highest NIR-II emission of Sb^{3+}/Tm^{3+}-codoped samples with a PLQY up to 48.9% was obtained when the Tm^{3+} ion feed concentration was 60%, as shown in Fig. S7.† Similarly, Te^{4+}/Tm^{3+}-codoped $Cs_2NaInCl_6$ also demonstrated a high NIR-II PLQY of up to 8.3% when the Tm^{3+} ion feed concentration was 50% (Fig. S8†). Based on the sensitization of Sb^{3+} or Te^{4+} ions, the NIR-II emission intensity of Sb^{3+}/Tm^{3+} and Te^{4+}/Tm^{3+} co-doped samples exhibited a huge improvement compared to the Tm^{3+} singly doped sample (Fig. 4b and d). The PLQY of NIR (NIR-I and NIR-II) emissions of Sb^{3+}/Tm^{3+}-codoped samples was up to 58.0%, while the NIR of Te^{4+}/Tm^{3+}-codoped samples showed a PLQY as high as 10.3%, showing excellent NIR luminescence performance. Note that the PLQY of NIR emission of this Sb^{3+}/Tm^{3+}-codoped $Cs_2NaInCl_6$ reaches the unprecedented 58.0%, which is the record in reported all-inorganic lead-free halide perovskites with a narrow NIR-II emission band (Table 1).

To determine the interaction between Tm^{3+} and Sb^{3+} (or Te^{4+}) dopants and the regulatory effect of Tm^{3+} on NIR emission, the PLE spectra of the Sb^{3+}/Tm^{3+}-doped sample moni-

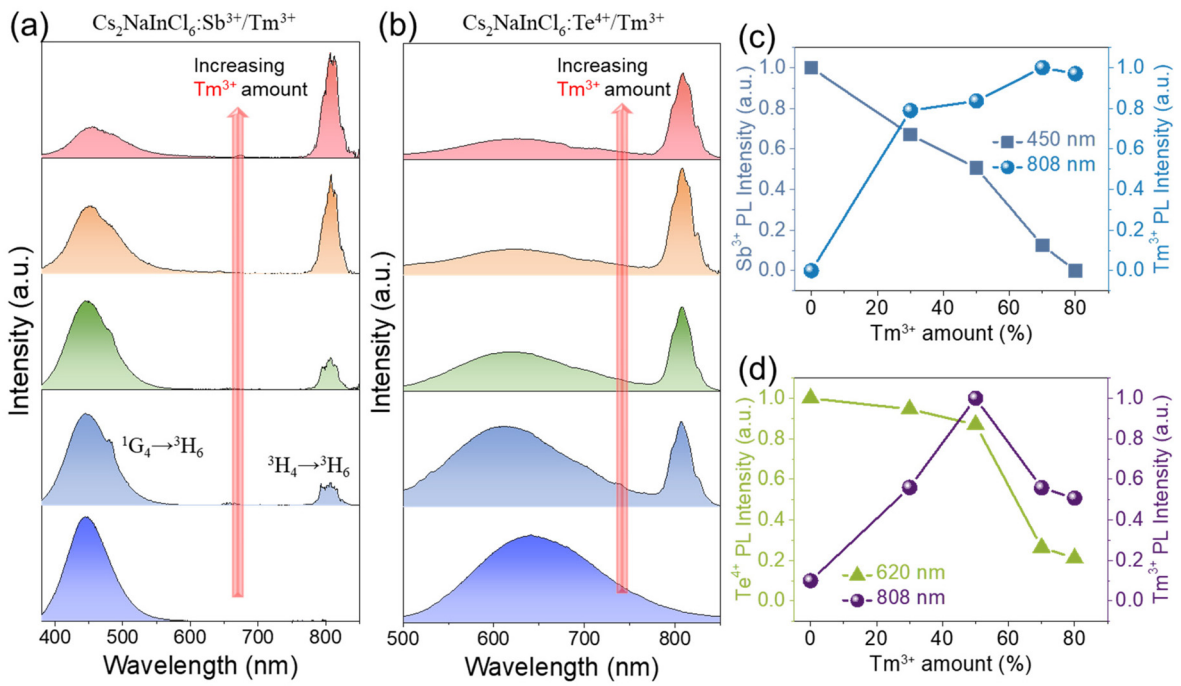

Fig. 3 PL spectra of (a) $Cs_2NaInCl_6$:Sb^{3+}/Tm^{3+} and (b) $Cs_2NaInCl_6$:Te^{4+}/Tm^{3+} with different Tm^{3+} ion concentrations, (c) 450 nm and 808 nm emission intensity of $Cs_2NaInCl_6$:Sb^{3+}/Tm^{3+} samples, and (d) 620 nm and 808 nm emission intensity of $Cs_2NaInCl_6$:Te^{4+}/Tm^{3+} samples.

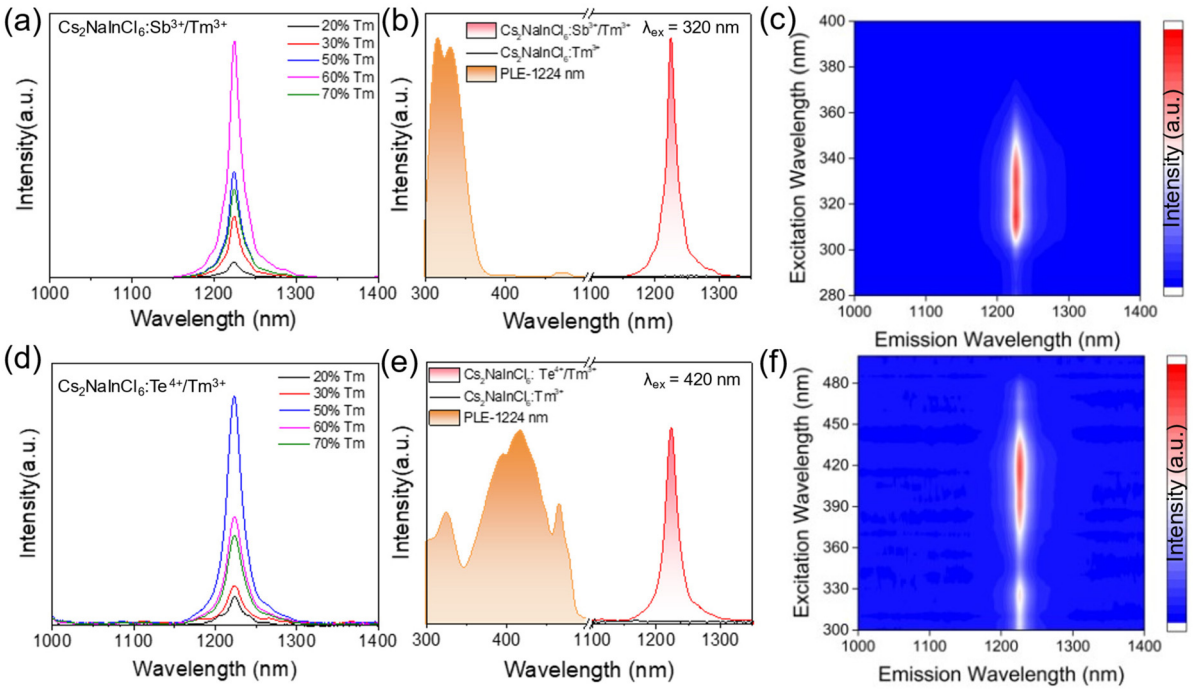

Fig. 4 (a) NIR-II emission spectra of $Cs_2NaInCl_6$:Sb^{3+}/Tm^{3+}. (b) PLE spectra of $Cs_2NaInCl_6$:5%Sb^{3+}/60%Tm^{3+}; PL spectra of $Cs_2NaInCl_6$:60%Tm^{3+} and $Cs_2NaInCl_6$:5%Sb^{3+}/60%Tm^{3+}. (c) Contour plot of the excitation-dependent NIR-II emission of $Cs_2NaInCl_6$:5%Sb^{3+}/60%Tm^{3+}. (d) NIR-II emission spectra of $Cs_2NaInCl_6$:1%Te^{4+}/50%Tm^{3+}. (e) PLE spectra of $Cs_2NaInCl_6$:1%Te^{4+}/50%Tm^{3+}; PL spectra of $Cs_2NaInCl_6$:50%Tm^{3+} and $Cs_2NaInCl_6$:1%Te^{4+}/50%Tm^{3+}. (f) Contour plot of the excitation-dependent NIR-II emission of $Cs_2NaInCl_6$:1%Te^{4+}/50%Tm^{3+}.

Table 1 Summary of the PL characteristics of NIR-emission lead-free metal halides

Compound	PLQY [%]	Excitation wavelength [nm]	Emission wavelength [nm]	Ref.
$Cs_2AgBiCl_6$:Yb^{3+}	—	365	1000	33
$Cs_2AgInCl_6$:Yb^{3+}	3.6	300	996	34
$Cs_2AgBiBr_6$:Yb^{3+}	28.0	430	1000	35
$Cs_2Ag_{0.2}Na_{0.8}BiCl_6$:$Yb^{3+}$	19.0	360	995	36
$Cs_2Ag_{0.2}Na_{0.8}BiCl_6$:$Er^{3+}$	4.3	360	1540	
Cs_2ZrCl_6:Te^{4+}/Yb^{3+}	0.2	392	1002	37
Cs_2ZrCl_6:Te^{4+}/Er^{3+}	6.1	392	1539	
$Cs_4MnBi_2Cl_{12}$:Yb^{3+}	1.4	360	1000	38
$Cs_2NaBiCl_6$:Mn^{2+}/Er^{3+}	14.2	360	1540	39
$Cs_2AgInCl_6$:Cr^{3+}	22.0	760	1010	40
$Cs_2AgInCl_6$:Cr^{3+}/Yb^{3+}	45.0	365	1000	41
$Cs_2NaSbCl_6$:Er^{3+}	0.3	335	1543	42
$Cs_2NaScCl_6$:Er^{3+}	28.3	365	1540	43
$Cs_2NaInCl_6$:Sb^{3+}/Tm^{3+}	58.0	320	808, 1224	**This work**
$Cs_2NaInCl_6$:Te^{4+}/Tm^{3+}	10.3	420	808, 1224	

tored at 450, 808 and 1224 nm and the PLE spectra of the Te^{4+}/Tm^{3+}-doped sample monitored at 620, 808 and 1224 nm were recorded (Fig. S9†). The PLE spectra of the $Cs_2NaInCl_6$:Sb^{3+}/Tm^{3+} sample at 450, 808 and 1224 nm were comparable (with the same excitation bands at 320 and 333 nm), providing evidence for the energy transfer from Sb^{3+} to Tm^{3+} ions.[14,44] Similar phenomena are observed in the PLE spectra of the $Cs_2NaInCl_6$:Te^{4+}/Tm^{3+} sample, indicating the presence of an energy transfer process. As shown in Fig. S9,† a weak narrow excitation peak at 470 nm, which is attributed to the direct excitation of Tm^{3+} ions ($^3H_6 \rightarrow {}^1G_4$ transition), was observed. As shown in Fig. S10,† the PL spectra of the $Cs_2NaInCl_6$:Sb^{3+}/Tm^{3+} or $Cs_2NaInCl_6$:Te^{4+}/Tm^{3+} sample display that the clear NIR emission peak still appears at different excitation wavelengths. The PLE spectra of visible and NIR emissions were comparable, which indicated that the excited state origin of these emission bands was the same. The emission of Tm^{3+} ions with f–f transitions is usually sensitive to the excitation wavelength, while the emission spectra are almost constant with the change in excitation wavelength, indicating that the NIR luminescence of Tm^{3+} ions mainly depends on the sensitization of Sb^{3+} or Te^{4+} ions. Moreover, the excitation intensity at 470 nm was lower than the excitation band of Sb^{3+} or Te^{4+} ions, indicating that the Tm excitation through the energy transfer was more efficient than direct excitation. Therefore, the energy transfer process through the ns^2 ion is the significant main pathway to achieve NIR emission of Tm^{3+} ions.

To determine the energy transfer process of $Cs_2NaInCl_6$:Sb^{3+}/Tm^{3+} and $Cs_2NaInCl_6$:Te^{4+}/Tm^{3+} samples, the time-resolved PL of ns^2 emissions were measured. As shown in Fig. 5a–d, the PL lifetimes monitored at 450 or 620 nm decreased with the increase in Tm^{3+} content (Tables S3 and S4†), indicating that the improved energy transfer from the ns^2 (at the $[SbCl_6]^{3-}$ or $[TeCl_6]^{2-}$ octahedron) to the Tm^{3+} ions pro-

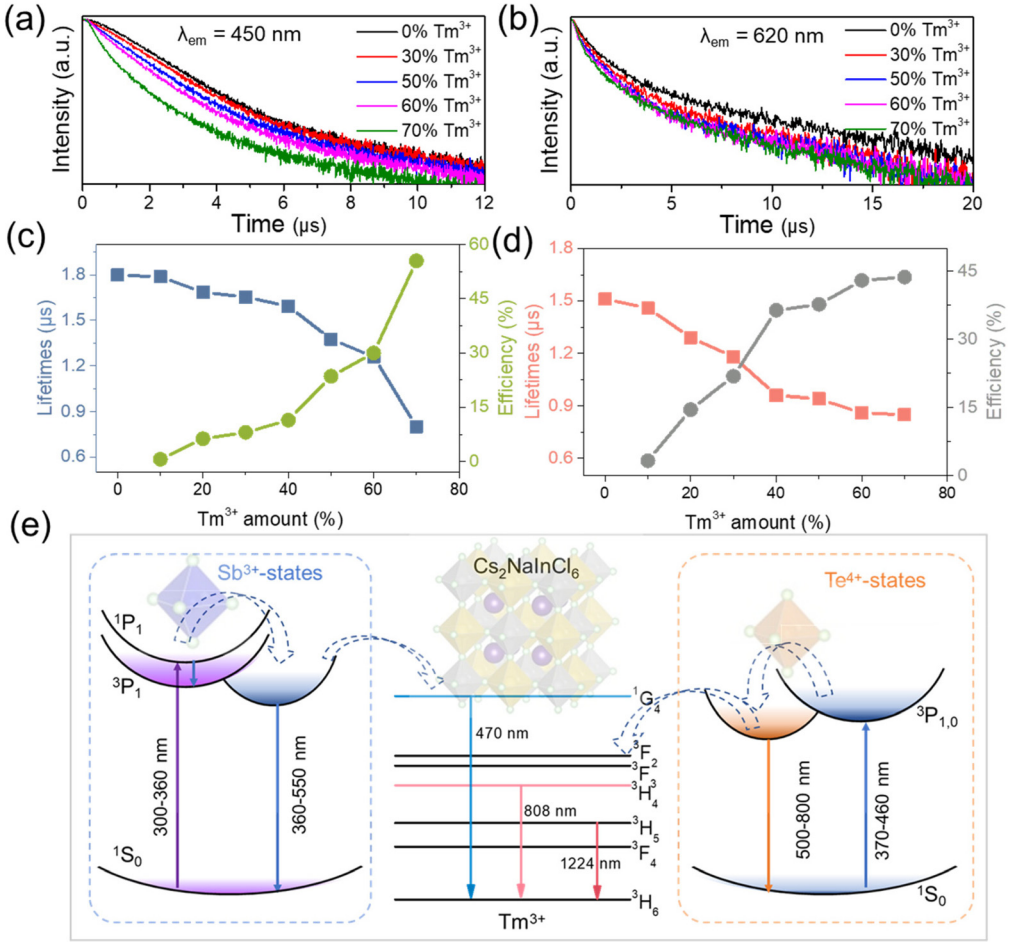

Fig. 5 PL lifetimes of (a) $Cs_2NaInCl_6$:Sb^{3+}/Tm^{3+} and (b) $Cs_2NaInCl_6$:Te^{4+}/Tm^{3+}. PL lifetimes (450 or 620 nm) and energy transfer efficiency as a function of Tm^{3+} concentration in (c) $Cs_2NaInCl_6$:Sb^{3+}/Tm^{3+} and (d) $Cs_2NaInCl_6$:Te^{4+}/Tm^{3+}. (e) Energy-level diagram of Sb^{3+}/Tm^{3+} and Te^{4+}/Tm^{3+} co-doped $Cs_2NaInCl_6$ and the proposed luminescence mechanism.

moted the decay of the ns^2 emission. The energy transfer efficiency (η_T) in the can be expressed as follows:[45]

$$\eta_T = 1 - \frac{\tau_x}{\tau_0}, \quad (1)$$

where τ_0 is the lifetime of ns^2 emission in the absence of Tm^{3+} ions and τ_x is the lifetime with different Tm^{3+} concentrations. The η_T values increase with the concentration of Tm^{3+} ions, reaching up 56.1% at 5%Sb^{3+}/70%Tm^{3+} doping and 43.7% at 1%Te^{4+}/70%Tm^{3+} doping (Fig. 5c and d). The efficient energy transfer efficiency can be attributed to the presence of Tm^{3+} and Sb^{3+} or Te^{4+} ions occupying the In^{3+} sites in the $Cs_2NaInCl_6$ lattice. This results in a reduced distance between the Sb^{3+} or Te^{4+} sensitizer and the Tm^{3+} activator, thereby favoring the occurrence probability of the energy transfer process. Moreover, for $Cs_2NaInCl_6$:Sb^{3+}/Tm^{3+}, a relatively large overlap between ns^2 emission and Tm^{3+} absorption profile (Fig. S11†) and a slight relaxation will facilitate the transfer of energy from Sb^{3+} to Tm^{3+}. The presence of the $^1G_4$ energy level (~470 nm) of Tm^{3+} ions is close to the emission of Sb^{3+} (~450 nm), which can act as a bridge to achieve a highly efficient energy transfer efficiency.

According to the above-mentioned investigations, the possible PL mechanism for $Cs_2NaInCl_6$:Sb^{3+}/Tm^{3+} and $Cs_2NaInCl_6$:Te^{4+}/Tm^{3+} is presented in Fig. 5e. For $Cs_2NaInCl_6$:Sb^{3+}/Tm^{3+}, the electrons can be excited from the ground state to the excited states of Sb^{3+} ions under 320 nm UV excitation, and then undergo a dynamic Jahn–Teller distortion, leading to broadband blue emission. After Bi^{3+} codoping, there is an increase in the splitting width of the PLE band, which can reduce the excitation energy to 330–390 nm range. The energy is then transferred to Tm^{3+} ions through the energy transfer channel from Sb^{3+} to Tm^{3+} ions, which results in the intrinsic emission of Tm^{3+} ions, achieving a blue emission at 470 nm (Tm^{3+}: $^1G_4 \rightarrow {}^3H_6$), an NIR-I emission at 808 nm (Tm^{3+}: $^3H_4 \rightarrow {}^3H_6$), and an NIR-II emission at 1224 nm (Tm^{3+}: $^3H_5 \rightarrow {}^3H_6$). Similarly, the electrons in the ground state of the $Cs_2NaInCl_6$:Te^{4+}/Tm^{3+} sample are excited to the excited state under low-energy blue light excitation, emitting a broadband emission at 500–800 nm through the inter-configurational transitions.

Meanwhile, some of the electrons are transferred to the $^3H_4$ and $^3H_5$ levels of Tm^{3+} ions, achieving an NIR-I emission at 808 nm and an NIR-II emission at 1224 nm. The doping of Tm^{3+} ions provides a pathway for efficient NIR-I and NIR-II emissions, while the selection of Sb^{3+} or Te^{4+} offers diverse sensitization routes.

To further unveil the photophysics process, density functional theory (DFT) calculations were carried out to determine the electronic structure of the $Cs_2NaInCl_6$:Sb^{3+}/Tm^{3+} and $Cs_2NaInCl_6$:Te^{4+}/Tm^{3+} systems, which are shown in Fig. 6. For the undoped $Cs_2NaInCl_6$ system, the conduction band minimum (CBM) is mainly composed of Cl p states and In s states, while the valence-band maximum (VBM) mainly consists of Cl p orbitals, as shown in Fig. S12.† In the Sb-doped system, a new band composed of the Sb lone-pair s states and Cl p states appears above the host valence band, while the $SbCl_6$ CBM emerges in a gap deep in the host conduction band, as shown in Fig. 6a. Similarly, the Te s states and Cl p states appear above the host valence band, while the $TeCl_6$ CBM emerges in front of the host conduction band (Fig. 6b). The $SbCl_6$ CBM–VBM gap (~3.7 eV) is higher than the $TeCl_6$ CBM–VBM gap (~3.3 eV), which matches the experimental results (a higher excitation energy for Sb than for Te). The calculations confirmed that the observed visible emission band originated from [$SbCl_6$] or [$TeCl_6$] octahedrons, respectively. Furthermore, as shown in Fig. 6c and d, the 4f bands of Tm are located in the CBM–VBM of $SbCl_6$ or $TeCl_6$, providing the possibility for the realization of energy transfer. These calculation results demonstrate that the introduced sensitizer Sb^{3+} or Te^{4+} ions can modulate the host electronic structure, while the introduced Tm^{3+} ions are located in the CBM–VBM of $SbCl_6$ or $TeCl_6$, which confirms the possibility of energy transfer.

To demonstrate the potential application of the NIR emission of $Cs_2NaInCl_6$:Sb/Tm and $Cs_2NaInCl_6$:Te/Tm materials, the simple NIR detection system is designed, as shown in Fig. 7a. The prepared $Cs_2NaInCl_6$:Sb^{3+}/Tm^{3+} samples were coated on a commercially available 310 nm UV-LED chip, while the $Cs_2NaInCl_6$:Te^{4+}/Tm^{3+} samples were coated on a commercially available 410 nm LED chip. The as-fabricated LED devices exhibited intense NIR luminescence, as shown in Fig. 7b. The intense NIR emissions demonstrate great potential in night vision applications, in which the photographs printed paper upon illumination with the NIR-LEDs as shown in Fig. 7c. Under natural light, photographs of the "Jiaying University" pattern were obtained using a visible camera. No image was captured by the cameras when the LEDs were off. In contrast, black-and-white images were recorded using an NIR

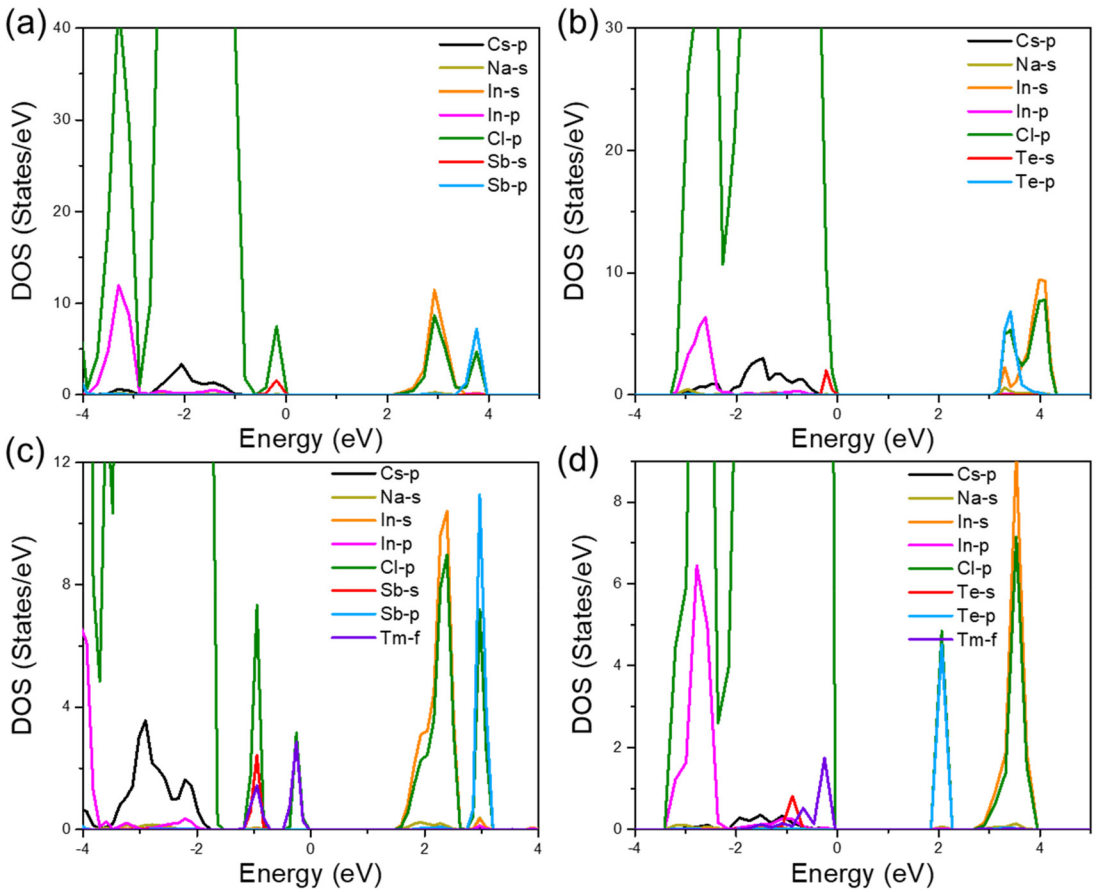

Fig. 6 Density of states (DOS) of (a) $Cs_2NaInCl_6$:Sb^{3+}, (b) $Cs_2NaInCl_6$:Te^{4+}, (c) $Cs_2NaInCl_6$:Sb^{3+}/Tm^{3+}, and (d) $Cs_2NaInCl_6$:Te^{4+}/Tm^{3+}.

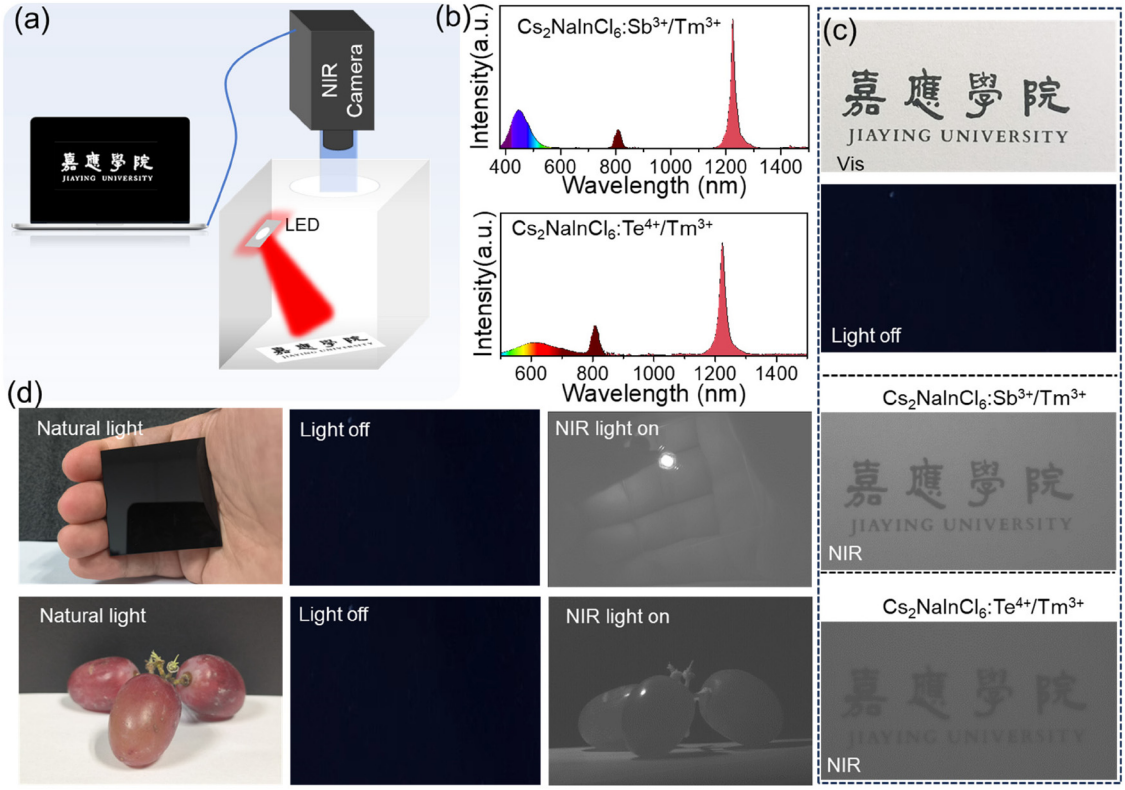

Fig. 7 (a) Schematic diagram of the NIR photography device. The LED is illuminated using a portable lamp colorimeter, and a 900 nm filter is installed at the LED light source to filter visible light. (b) Emission spectra of the as-fabricated NIR emitting LED composed of $Cs_2NaInCl_6$:5%Sb^{3+}/60%Tm^{3+} and $Cs_2NaInCl_6$:1%Te^{4+}/50%Tm^{3+} phosphors. (c) Photographs under daylight, in the darkness, and upon illumination with the NIR LED. (d) Vis and NIR images illuminated by fluorescent light and the fabricated NIR LED light.

camera when the NIR LEDs were ignited. The fabricated NIR LED can also be used for night vision surveillance and penetration applications by virtue of the unique spectral characteristics of NIR-II light, such as being invisible to the naked eye and special penetration ability. Under natural light, part of the emission band covered by the 750 nm filter was not detected by the visible camera. When the NIR LED is turned on, the obscured hand is clear in the NIR camera (Fig. 7d). Furthermore, the strong NIR emission enables a clear fruit image by the NIR camera under the irradiation of an NIR LED lamp, which reveals the great potential of the prepared samples in night vision technologies and other related fields. The Tm^{3+}-doped NIR materials also exhibit excellent environmental stability, which does not degrade significantly after 2 months, and the luminescence intensity is basically consistent with the original value under ambient conditions (Fig. S13a and b†). The XRD measurements showed that the Tm^{3+}-doped sample structure can remain stable for more than 90 days (Fig. S13c and d†). Moreover, the PL performances of $Cs_2NaInCl_6$:Sb^{3+}/Tm^{3+} and $Cs_2NaInCl_6$:Te^{4+}/Tm^{3+} samples were almost unchanged even upon heating at 400 K for 6 h, demonstrating excellent thermal stability, as shown in Fig. S14.† These results demonstrated that Tm^{3+}-doped perovskites are promising for NIR LED in advanced night vision detection.

Conclusions

In summary, $Cs_2NaInCl_6$:Sb^{3+}/Tm^{3+} and $Cs_2NaInCl_6$:Te^{4+}/Tm^{3+} single crystals have been successfully synthesized, which enable efficient NIR-I and NIR-II emissions. $Cs_2NaInCl_6$:Sb^{3+}/Tm^{3+} shows efficient blue emissions at 450 nm, and an NIR-I emission peak at 808 nm and an NIR-II emission peak at 1224 nm under 320 nm excitation, while $Cs_2NaInCl_6$:Te^{4+}/Tm^{3+} exhibits broadband orange emissions at 620 nm, and similar NIR-I and NIR-II emission peaks at 808 and 1224 nm under 420 nm excitation. A high NIR (NIR-I and NIR-II) PLQY of up to 58.0% was obtained in $Cs_2NaInCl_6$:Sb^{3+}/Tm^{3+}, while a high NIR PLQY of up to 10.3% was obtained in $Cs_2NaInCl_6$:Te^{4+}/Tm^{3+}. The experiments and theoretical calculations reveal the origin of the luminescence as well as demonstrate the possibility of energy transfer. The efficient energy transfer channel design from Sb^{3+} enables us to realize efficient NIR emissions, and the energy transfer channel from Te^{4+} enables us to realize long-wavelength low-energy excited NIR emission. The excellent optical performance combined with excellent environmental stability makes Tm^{3+}-doped halide perovskites have a good application in NIR LED and night-vision devices. These findings provide a design strategy to tune the excited state based on different sensitizers, which can achieve efficient

infrared emission under different excitation energies for versatile photoelectric applications.

Data availability

The data supporting this article have been included as part of the ESI.†

Conflicts of interest

The authors declare no conflict of interest.

Acknowledgements

This work was supported by the University Key Laboratory of Guangdong (2024KSYS021), Universities Special Project in Key Fields of Guangdong (no. 2022ZDZX3027), Natural Science Foundation of Guangdong Province (no. 2022A1515010813), University Engineering Technology Center of Guangdong (no. 2022GCZX007), Inorganic Optical Functional Materials and Application Innovation Team of Guangdong (no. 2023KCXTD033).

References

1 Y. Liu, F. Di Stasio, C. Bi, J. Zhang, Z. Xia, Z. Shi and L. Manna, Near-Infrared Light Emitting Metal Halides: Materials, Mechanisms, and Applications, *Adv. Mater.*, 2024, **36**, 2312482.
2 F. Yuan, G. Folpini, T. Liu, U. Singh, A. Treglia, J. W. M. Lim, J. Klarbring, S. I. Simak, I. A. Abrikosov, T. C. Sum, A. Petrozza and F. Gao, Bright and stable near-infrared lead-free perovskite light-emitting diodes, *Nat. Photonics*, 2024, **18**, 170–176.
3 G. Liu, W. Chen, Z. Xiong, Y. Wang, S. Zhang and Z. Xia, Laser-driven broadband near-infrared light source with watt-level output, *Nat. Photonics*, 2024, **18**, 562–568.
4 C. Li, Y. Pang, Y. Xu, M. Lu, L. Tu, Q. Li, A. Sharma, Z. Guo, X. Li and Y. Sun, Near-infrared metal agents assisting precision medicine: from strategic design to bioimaging and therapeutic applications, *Chem. Soc. Rev.*, 2023, **52**, 4392–4442.
5 J. Qiao, G. Zhou, Y. Zhou, Q. Zhang and Z. Xia, Divalent europium-doped near-infrared-emitting phosphor for light-emitting diodes, *Nat. Commun.*, 2019, **10**, 5267.
6 M. Lukovic, V. Lukovic, I. Belca, B. Kasalica, I. Stanimirovic and M. Vicic, LED-based Vis-NIR spectrally tunable light source - the optimization algorithm, *J. Eur. Opt. Soc., Rapid Publ.*, 2016, **12**, 19.
7 H. Yu, J. Chen, R. Mi, J. Yang and Y.-G. Liu, Broadband near-infrared emission of K_3ScF_6:Cr^{3+} phosphors for night vision imaging system sources, *Chem. Eng. J.*, 2021, **417**, 129271.
8 Q. Zhang, X. Wei, J. Zhou, B. Milićević, L. Lin, J. Huo, J. Li, H. Ni and Z. Xia, Thermal Stability Improvement of Cr^{3+}-Activated Broadband Near-Infrared Phosphors via State Population Optimization, *Adv. Opt. Mater.*, 2023, **11**, 2300310.
9 Y. Zhou, X. Li, T. Seto and Y. Wang, A High Efficiency Trivalent Chromium-Doped Near-Infrared-Emitting Phosphor and Its NIR Spectroscopy Application, *ACS Sustainable Chem. Eng.*, 2021, **9**, 3145–3156.
10 S. Miao, Y. Liang, D. Chen, R. Shi, X. Shan, Y. Zhang, F. Xie and X.-J. Wang, Site-Selective Occupancy Control of Cr Ions toward Ultrabroad-Band Infrared Luminescence with a Spectral Width up to 419 nm, *ACS Appl. Mater. Interfaces*, 2022, **14**, 53101–53110.
11 Y. Wang, Z. Wang, G. Wei, Y. Yang, S. He, J. Li, Y. Shi, R. Li, J. Zhang and P. Li, Ultra-Broadband and high efficiency Near-Infrared $Gd_3Zn_xGa_{5-2x}Ge_xO_{12}$:$Cr^3$+ (x = 0–2.0) garnet phosphors via crystal field engineering, *Chem. Eng. J.*, 2022, **437**, 135346.
12 X. Dai, X. Zou, H. Zhang, W. Chen, C. Yang, M. S. Molokeev, Z. Xia, Y. Liu, X. Zhang, M. Zheng and B. Lei, Novel Cr^{3+}-Doped Garnet Phosphor with Broadband Efficient Far-Red Emission for Photochrome Matching Plant-Lighting, *Adv. Opt. Mater.*, 2024, **12**, 2302380.
13 R. Marin and D. Jaque, Doping Lanthanide Ions in Colloidal Semiconductor Nanocrystals for Brighter Photoluminescence, *Chem. Rev.*, 2021, **121**, 1425–1462.
14 J. Nie, B. Zhou, S. Fang, H. Zhong, H. Li and Y. Shi, Efficient Multicolor and White Photoluminescence in Erbium- and Holmium-Incorporated $Cs_2NaInCl_6$:Sb^{3+} Double Perovskites, *Chem. Mater.*, 2022, **34**, 6288–6295.
15 L. Liang, J. Chen, K. Shao, X. Qin, Z. Pan and X. Liu, Controlling persistent luminescence in nanocrystalline phosphors, *Nat. Mater.*, 2023, **22**, 289–304.
16 G. Pan, X. Bai, D. Yang, X. Chen, P. Jing, S. Qu, L. Zhang, D. Zhou, J. Zhu, W. Xu, B. Dong and H. Song, Doping Lanthanide into Perovskite Nanocrystals: Highly Improved and Expanded Optical Properties, *Nano Lett.*, 2017, **17**, 8005–8011.
17 Y. Mahor, W. J. Mir and A. Nag, Synthesis and Near-Infrared Emission of Yb-Doped $Cs_2AgInCl_6$ Double Perovskite Microcrystals and Nanocrystals, *J. Phys. Chem. C*, 2019, **123**, 15787–15793.
18 X. Li, X. Shen, M. Lu, J. Wu, Y. Zhong, Z. Wu, W. W. Yu, Y. Gao, J. Hu, J. Zhu, Y. Zhang and X. Bai, Wide-coverage and Efficient NIR Emission from Single-component Nanophosphors through Shaping Multiple Metal-halide Packages, *Angew. Chem., Int. Ed.*, 2023, **62**, e202217832.
19 L. Cao, X. Jia, W. Gan, C.-G. Ma, J. Zhang, B. Lou and J. Wang, Strong Self-Trapped Exciton Emission and Highly Efficient Near-Infrared luminescence in Sb^{3+}-Yb^{3+} Co-doped $Cs_2AgInCl_6$ Double Perovskite, *Adv. Funct. Mater.*, 2023, **33**, 2212135.
20 W. J. Mir, T. Sheikh, H. Arfin, Z. Xia and A. Nag, Lanthanide doping in metal halide perovskite nanocrystals: spectral shifting, quantum cutting and optoelectronic applications, *NPG Asia Mater.*, 2020, **12**, 9.

21 Z. Zeng, B. Huang, X. Wang, L. Lu, Q. Lu, M. Sun, T. Wu, T. Ma, J. Xu, Y. Xu, S. Wang, Y. Du and C.-H. Yan, Multimodal Luminescent $Yb^{3+}/Er^{3+}/Bi^{3+}$-Doped Perovskite Single Crystals for X-ray Detection and Anti-Counterfeiting, *Adv. Mater.*, 2020, **32**, 2004506.

22 S. Han, D. Tu, Z. Xie, Y. Zhang, J. Li, Y. Pei, J. Xu, Z. Gong and X. Chen, Unveiling Local Electronic Structure of Lanthanide-Doped $Cs_2NaInCl_6$ Double Perovskites for Realizing Efficient Near-Infrared Luminescence, *Adv. Sci.*, 2022, **9**, 2203735.

23 Y. Wang, P. Dang, L. Qiu, G. Zhang, D. Liu, Y. Wei, H. Lian, G. Li, Z. Cheng and J. Lin, Multimode Luminescence Tailoring and Improvement of $Cs_2NaHoCl_6$ Cryolite Crystals via Sb^{3+}/Yb^{3+} Alloying for Versatile Photoelectric Applications, *Angew. Chem., Int. Ed.*, 2023, **62**, e202311699.

24 W. Gan, L. Cao, S. Gu, H. Lian, Z. Xia and J. Wang, Broad-Band Sensitization in Cr^{3+}–Er^{3+} Co-Doped $Cs_2AgInCl_6$ Double Perovskites with 1.5 μm Near-Infrared Emission, *Chem. Mater.*, 2023, **35**, 5291–5299.

25 H. Arfin, J. Kaur, T. Sheikh, S. Chakraborty and A. Nag, Bi^{3+}-Er^{3+} and Bi^{3+}-Yb^{3+} Codoped $Cs_2AgInCl_6$ Double Perovskite Near-Infrared Emitters, *Angew. Chem., Int. Ed.*, 2020, **59**, 11307–11311.

26 S. Saikia, A. Joshi, H. Arfin, S. Badola, S. Saha and A. Nag, Sb^{3+}–Er^{3+}-Codoped $Cs_2NaInCl_6$ for Emitting Blue and Short-Wave Infrared Radiation, *Angew. Chem., Int. Ed.*, 2022, **61**, e202201628.

27 S. Jin, R. Li, H. Huang, N. Jiang, J. Lin, S. Wang, Y. Zheng, X. Chen and D. Chen, Compact ultra-broadband light-emitting diodes based on lanthanide doped lead-free double perovskites, *Light: Sci. Appl.*, 2022, **11**, 52.

28 J. Nie, H. Li, S. Fang, B. Zhou, Z. Liu, F. Chen, Y. Wang and Y. Shi, Efficient red photoluminescence in holmium-doped $Cs_2NaInCl_6$ double perovskite, *Cell Rep. Phys. Sci.*, 2022, **3**, 100820.

29 Y. Y. Jing, Y. Liu, M. Z. Li and Z. G. Xia, Photoluminescence of Singlet/Triplet Self-Trapped Excitons in Sb^{3+}-Based Metal Halides, *Adv. Opt. Mater.*, 2021, **9**, 2002213.

30 H. Arfin, R. Rathod, A. S. Shingote, K. R. Priolkar, P. K. Santra and A. Nag, Short-Wave Infrared Emissions from Te^{4+}–Ln^{3+} (Ln: Er, Yb)-Codoped $Cs_2NaInCl_6$ Double Perovskites, *Chem. Mater.*, 2023, **35**, 7133–7143.

31 W. Zhang, W. Zheng, L. Li, P. Huang, Z. Gong, Z. Zhou, J. Sun, Y. Yu and X. Chen, Dual-Band-Tunable White-Light Emission from Bi^{3+}/Te^{4+} Emitters in Perovskite-Derivative Cs_2SnCl_6 Microcrystals, *Angew. Chem., Int. Ed.*, 2022, **61**, e202116085.

32 Z. Gong, W. Zheng, P. Huang, X. Cheng, W. Zhang, M. Zhang, S. Han and X. Chen, Highly efficient Sb^{3+} emitters in 0D cesium indium chloride nanocrystals with switchable photoluminescence through water-triggered structural transformation, *Nano Today*, 2022, **44**, 101460.

33 N. Chen, T. Cai, W. Li, K. Hills-Kimball, H. Yang, M. Que, Y. Nagaoka, Z. Liu, D. Yang, A. Dong, C.-Y. Xu, R. Zia and O. Chen, Yb- and Mn-Doped Lead-Free Double Perovskite Cs_2AgBiX_6 (X = Cl–, Br–) Nanocrystals, *ACS Appl. Mater. Interfaces*, 2019, **11**, 16855–16863.

34 W. Lee, S. Hong and S. Kim, Colloidal Synthesis of Lead-Free Silver–Indium Double-Perovskite $Cs_2AgInCl_6$ Nanocrystals and Their Doping with Lanthanide Ions, *J. Phys. Chem. C*, 2019, **123**, 2665–2672.

35 F. Schmitz, K. Guo, J. Horn, R. Sorrentino, G. Conforto, F. Lamberti, R. Brescia, F. Drago, M. Prato, Z. He, U. Giovanella, F. Cacialli, D. Schlettwein, D. Meggiolaro and T. Gatti, Lanthanide-Induced Photoluminescence in Lead-Free $Cs_2AgBiBr_6$ Bulk Perovskite: Insights from Optical and Theoretical Investigations, *J. Phys. Chem. Lett.*, 2020, **11**, 8893–8900.

36 Y. Pei, D. Tu, C. Li, S. Han, Z. Xie, F. Wen, L. Wang and X. Chen, Boosting Near-Infrared Luminescence of Lanthanide in $Cs_2AgBiCl_6$ Double Perovskites via Breakdown of the Local Site Symmetry, *Angew. Chem., Int. Ed.*, 2022, **61**, e202205276.

37 J. Sun, W. Zheng, P. Huang, M. Zhang, W. Zhang, Z. Deng, S. Yu, M. Jin and X. Chen, Efficient Near-Infrared Luminescence in Lanthanide-Doped Vacancy-Ordered Double Perovskite Cs_2ZrCl_6 Phosphors via Te^{4+} Sensitization, *Angew. Chem., Int. Ed.*, 2022, **61**, e202201993.

38 J. Li, J. Xiao, T. Lin, Z. Yan and X. Han, Lanthanide doping enabled multimodal luminescence in layered lead-free double perovskite $Cs_4MnBi_2Cl_{12}$, *J. Mater. Chem. C*, 2022, **10**, 7626–7632.

39 W. Gan, B.-M. Liu, L. Huang, S. Lou, J. Zhang, Z. Zhou and J. Wang, Manganese Ion-Sensitized Near-Infrared Light in $Cs_2NaBi_{1-x}Er_xCl_6$ Lead-Free Double Perovskite, *Adv. Opt. Mater.*, 2022, **10**, 2102851.

40 F. Zhao, Z. Song, J. Zhao and Q. Liu, Double perovskite $Cs_2AgInCl_6$:Cr^{3+}: broadband and near-infrared luminescent materials, *Inorg. Chem. Front.*, 2022, **9**, 4695–4704.

41 D. Chen, X. Zhang, J. Wei, L. Zhou, P. Chen, Q. Pang and J. Z. Zhang, Simultaneous enhancement of near infrared luminescence and stability of $Cs_2AgInCl_6$:Cr^{3+} double perovskite single crystals enabled by a Yb^{3+} dopant, *Inorg. Chem. Front.*, 2022, **9**, 4695–4704.

42 R. Wu, P. Han, D. Zheng, J. Zhang, S. Yang, Y. Zhao, X. Miao and K. Han, All-Inorganic Rare-Earth-Based Double Perovskite Nanocrystals with Near-Infrared Emission, *Laser Photonics Rev.*, 2021, **15**, 2100218.

43 C. Zhao, Y. Gao, T. Song, J. Wang and J. Qiu, An Er^{3+}-Doped $Cs_2NaScCl_6$ Lead-Free Double Perovskite with Efficient Broadband Visible to Near-Infrared Emission and Multimodal Upconversion Luminescence, *J. Phys. Chem. Lett.*, 2023, **14**, 9011–9018.

44 M. Cong, Q. Zhang, B. Yang, J. Chen, J. Xiao, D. Zheng, T. Zheng, R. Zhang, G. Qing, C. Zhang and K.-L. Han, Bright Triplet Self-Trapped Excitons to Dopant Energy Transfer in Halide Double-Perovskite Nanocrystals, *Nano Lett.*, 2021, **21**, 8671–8678.

45 Y. Liu, X. Rong, M. Li, M. S. Molokeev, J. Zhao and Z. Xia, Incorporating Rare-Earth Terbium(III) Ions into $Cs_2AgInCl_6$:Bi Nanocrystals toward Tunable Photoluminescence, *Angew. Chem., Int. Ed.*, 2020, **59**, 11634–11640.